Yuqun Lan
State Key Laboratory of Nonlinear Mechanics,
Institute of Mechanics,
Chinese Academy of Sciences,
Beijing 100190, China;
School of Engineering Science,
University of Chinese Academy of Sciences,
Beijing 100049, China
e-mail: lanyuqun@imech.ac.cn

Guodong Liu
State Key Laboratory of Nonlinear Mechanics,
Institute of Mechanics,
Chinese Academy of Sciences,
Beijing 100190, China;
School of Engineering Science,
University of Chinese Academy of Sciences,
Beijing 100049, China
e-mail: iamlgd2021@163.com

Shizhen Yin
State Key Laboratory of Nonlinear Mechanics,
Institute of Mechanics,
Chinese Academy of Sciences,
Beijing 100190, China;
School of Engineering Science,
University of Chinese Academy of Sciences,
Beijing 100049, China
e-mail: sy5gn@virginia.edu

Yang Zhao
State Key Laboratory of Nonlinear Mechanics,
Institute of Mechanics,
Chinese Academy of Sciences,
Beijing 100190, China;
School of Engineering Science,
University of Chinese Academy of Sciences,
Beijing 100049, China
e-mail: zhaoyang@imech.ac.cn

Chong Liu
School of Engineering Science,
University of Chinese Academy of Sciences,
Beijing 100049, China;
State Key Laboratory of High-Temperature Gas
Dynamics, Institute of Mechanics,
Chinese Academy of Sciences,
Beijing 100190, China
e-mail: chongliu@imech.ac.cn

Lijuan Sun
State Key Laboratory of Nonlinear Mechanics,
Institute of Mechanics,
Chinese Academy of Sciences,
Beijing 100190, China;
School of Engineering Science,
University of Chinese Academy of Sciences,
Beijing 100049, China
e-mail: sunlj@lnm.imech.ac.cn

One-Step Patterned Contact-Resistance-Free Stretchable Strain Sensors With High Linearity and Repeatability for Body-Motion Detection

Most of the resistive-type stretchable strain sensors exhibit large sensing ranges and high sensitivity but suboptimal repeatability and linearity because of the contact-resistance mechanism. To achieve high repeatability and linearity, several sensors with contact-resistance-free structures are proposed. However, due to the different geometric layouts of the conductive materials and the insulating substrates, the patterning of these sensors requires multiple processes including photolithography and etching, which may cause high costs and are not suitable for consumer wearable applications. Here, we report a design for stretchable strain sensors based on a one-step patterned contact-resistance-free structure, i.e., the independent-sensing-and-stretchable-function structure (ISSFS). The stretchability mainly comes from the overall large deformation of the wide curved segments (the stretchable parts), while the resistance variation is mainly attributed to the tensile strain of the narrow straight segments (the sensing parts). High linearity ($R^2 = 0.999$) and repeatability (repeatability error $= 1.44\%$) are achieved because neither unstable contact resistance nor nonlinear constitutive and geometric behaviors occur during the sensing process. The conductive materials and the insulating substrates do not need to have different geometric layouts; thus, they can be patterned by only one-step laser cutting. The proposed sensors show great potential in body-motion detection for wearable devices. [DOI: 10.1115/1.4056766]

Keywords: stretchable strain sensors, high linearity, high repeatability, laser cutting, elasticity, structures

---

Shuang Li[1]
State Key Laboratory of Nonlinear Mechanics,
Institute of Mechanics,
Chinese Academy of Sciences,
Beijing 100190, China;
School of Engineering Science,
University of Chinese Academy of Sciences,
Beijing 100049, China
e-mail: lishuang@lnm.imech.ac.cn

Yewang Su[1]
State Key Laboratory of Nonlinear Mechanics,
Institute of Mechanics,
Chinese Academy of Sciences,
Beijing 100190, China;
School of Engineering Science,
University of Chinese Academy of Sciences,
Beijing 100049, China
e-mail: yewangsu@imech.ac.cn

1 Introduction

Over the last decade, flexible electronics integrated with various sensors, including strain sensors [1–8], pressure sensors [9–14], and temperature sensors [15–17], have broken through the limitation of traditional rigid electronics and have profoundly changed the mode of industrial production and human lifestyles [18]. In particular, strain sensors with large sensing ranges are required to allow the monitoring of the body deformation and motion in applications of health monitoring [1,19,20], human–computer interaction [21–23], and eXtended Reality (XR) [8,24]. However, limited by poor mechanical compliance and narrow sensing ranges [8,25,26], conventional strain gauges cannot meet the growing requirements. Intensive efforts have been made to develop new-type stretchable strain sensors based on capacitive [2,27], resistive [1,21], piezoelectric [28,29], and triboelectric [30] effects. Among them, the resistive-type stretchable strain sensor is widely used for its simple sensing mechanism and capability of anti-jamming [31].

Most of the resistive-type stretchable strain sensors adopted the contact-resistance mechanism to achieve a large sensing range and a high sensitivity [3,6,32–35]. The designed conductive microstructures include the prestrained conductive material array [36,37], spring-like structure [6,32,38], fish-scale-like structure [5,39], island-gap structure [40,41], crack [7,20,42,43], etc. The adopted conductive materials include metal membranes/nanowires/nanoparticles [7,22,43,44], carbon-based materials [3,20,23,41,44], and conductive polymer [35,45]. However, many of these sensors have the problems of suboptimal linearity and repeatability caused by the unstable contact resistance and nonlinear constitutive/geometric behaviors during the sensing process [46]. Considering that the installation regime of the sensor is not always strain-free, the strain sensors with suboptimal linearity cannot guarantee the applicability of the calibration relationship after the operation of zero clearing [47]. The suboptimal repeatability can also bring undesirable measurement errors in multiple measurements under the same applied strain. Therefore, such sensors would run into the plight of complicated calibration and the risk of large measurement errors in practical applications.

To achieve high repeatability and linearity, researchers recently proposed several stretchable strain sensors with the contact-resistance-free structures where the resistance variation is caused by the elastic deformation of conductive metal materials [19,46]. For example, Li et al. presented an off-axis serpentine sandwich structure with the mechanism of the stretch−bending−stretch transformation as one of the contact-resistance-free structures to achieve high repeatability (repeatability error = 1.58%) and linearity

(coefficient of determination > 0.999) [46]. These strain sensors have contributed a lot to the high-precise measurement in the medical and aerospace fields. However, due to the different geometric layouts of the conductive metal materials (e.g., gold) and the insulating substrates (e.g., polyimide), the patterning of these sensors [19,46,48,49] requires multiple processes including photolithography, etching, and laser cutting. Besides, the sensors need to be transferred among different processing platforms to complete the whole fabrication process, which requires an ultraclean room and a high degree of re-positioning accuracy of the processing platforms. These strict factors dramatically increase the manufacturing cost of consumer wearable applications and thus prevent them from popularization. In addition, limited by the photolithography process, the length of the fabricated sensors is typically less than 30 cm, which is unfavorable for the average strain measurements over a large size range such as the waistline, thigh circumference, and arm circumference during exercise.

Here, we report a design for stretchable strain sensors based on another kind of microfabricated contact-resistance-free structure, i.e., the independent-sensing-and-stretchable-function structure (ISSFS). The stretchability mainly comes from the overall large deformation of the wide curved segments (the stretchable parts), while the resistance variation mainly comes from the tensile strain of the narrow straight segments (the sensing parts). Therefore, the conductive metal materials and the insulating substrates do not need to have different geometric layouts, and the patterning process can be completed by only one step of laser cutting. High linearity ($R^2 = 0.999$) and repeatability (repeatability error = 1.44%) are achieved because neither unstable contact resistance nor nonlinear constitutive and geometric behaviors would occur during the sensing process. The consistency of the electrical responses in different stretching modes is verified to ensure accurate measurement in practical applications. Furthermore, a design of temperature self-compensation is proposed to free the sensor from the influence of temperature. The present sensors show great application potential in medical surgery, intelligent devices, and motion monitoring. The design idea of the ISSFS can be extended to stretchable strain sensors with high accuracy and other special advantages by employing different conductive materials.

2 Results and Discussion

2.1 Design and Fabrication. Figure 1(a) illustrates an exploded view of the designed strain sensor, consisting of an ISSFS and the bottom and top encapsulation layers. The ISSFS is
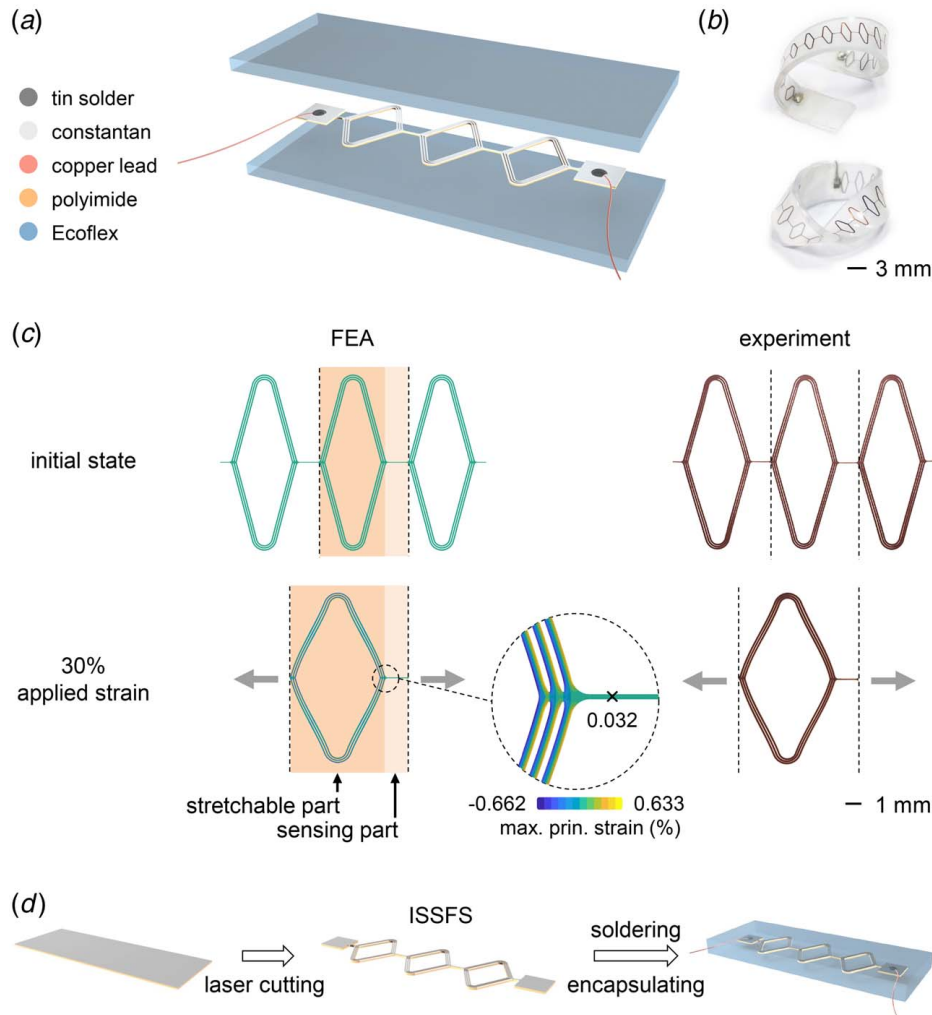
Fig. 1 Strain sensor based on the ISSFS: (a) exploded view of the strain sensor, (b) bending and twisting of a fabricated strain sensor, (c) FEA and experimental results shown in the top view for an ISSFS in the initial state and stretched by 30% applied strain (inset: enlarged view of maximum principal strain distribution near the joint of the stretchable part and the sensing part), and (d) illustration of the fabrication processes

composed of a patterned conductive layer (constantan foil in this work for its low resistance temperature coefficient) with two connection pads soldered to external leads, and a polyimide (PI) substrate with the same pattern. A soft silicone material (Ecoflex 00-30, Smooth-On, PA, USA) is employed to form the top and bottom encapsulation layers. As shown in Fig. 1(b), the fabricated strain sensor can be easily bent or twisted, indicating its excellent flexibility.

Figure 1(c) shows the results of the finite element analysis (FEA) and the experiment of the ISSFS stretched by 30% applied strain. The agreement of the overall deformation predicted by FEA with the experiment results validates the reliability of FEA as a tool to understand the sensing mechanism. The ISSFS can be divided into several stretchable parts (the wide curved segments) and sensing parts (the narrow straight segments) connected in series. The stretchability is mainly attributed to the stretchable parts. The design of the thick PI makes the thickness in the same order as the width. Thus, the stretchable parts will undergo mainly in-plane deformation when stretched [50] and transform the overall large displacement into small bending and rotation. While the resistance variation mainly comes from the tensile strain of the sensing parts, their linear elongation can derive a linear increment in resistance. Owing to the combination of the two parts with different functions, neither unstable contact resistance nor nonlinear constitutive and geometric behaviors would occur

during the sensing process. Therefore, the stretchable strain sensor based on the ISSFS could have large stretchability, high linearity, and high repeatability simultaneously.

The fabrication processes of the strain sensor can be realized by standard planar micro-fabrication strategies including laser cutting and encapsulation (Fig. 1(d), details are shown in the Experimental Section). The aforementioned design idea of the ISSFS enables the conductive metal materials and the insulating substrates to share the same geometric layouts. Hence, the double-layer material (a 5-μm-thick constantan and a 200-μm-thick PI) can be patterned into ISSFS with an ultraviolet picosecond laser in one step. After that, the ISSFS is soldered for connection to an external circuit and encapsulated by the soft silicone material (Ecoflex). The length of the strain sensor can be customized from a few to several tens of centimeters per the above process. All of these processes are industrially mature, low in cost, and have no requirements for the ultraclean room, which is favorable for mass production and consumer wearable applications.

2.2 Mechanical and Electrical Characterization of ISSFS. A mechanical model of ISSFS is established for the quantitative analysis and design optimization (Fig. 2(a) and Fig. S1 (available in the Supplemental Materials on the ASME Digital Collection)). Given the symmetry of geometry and loads, a quarter of the
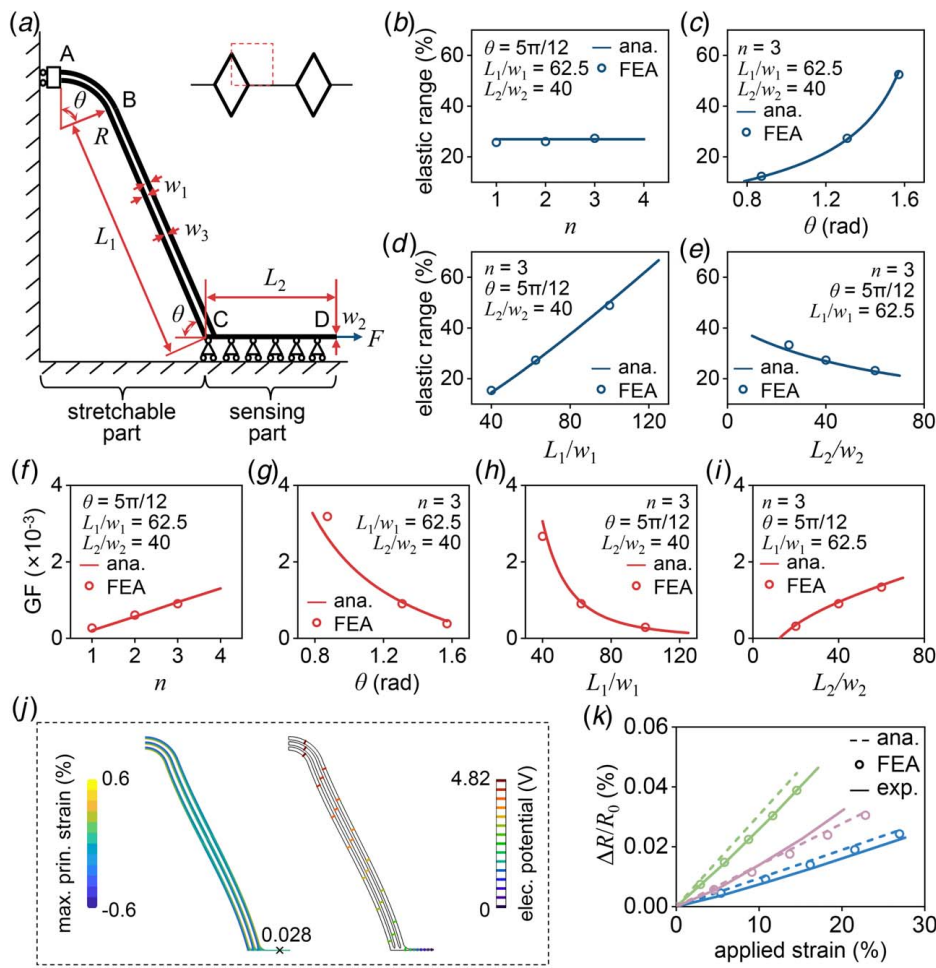
Fig. 2 Theoretical analysis of the ISSFS: (*a*) Mechanical model of the ISSFS under stretch. (*b*) Effects of dimensionless parameters R/w_1 on the elastic range. (*c*) Effects of dimensionless parameters θ on the elastic range. (*d*) Effects of dimensionless parameters L_1/w_1 on the elastic range. (*e*) Effects of dimensionless parameters L_2/w_2 on the elastic range. (*f*) Effects of dimensionless parameters R/w_1 on GF. (*g*) Effects of dimensionless parameters θ on GF. (*h*) Effects of dimensionless parameters L_1/w_1 on GF. (*i*) Effects of dimensionless parameters L_2/w_2 on GF. (*j*) Plot of maximal principal strain field and contour plot of electric potential of the conductive layer. (*k*) Relative resistance changes versus the applied strain with $\bar{\lambda}_1 = 40$ and $\bar{\lambda}_2 = 40$ for the green dataset; $\bar{\lambda}_1 = 62.5$ and $\bar{\lambda}_2 = 60$ for the lavender dataset; $\bar{\lambda}_1 = 62.5$ and $\bar{\lambda}_2 = 40$ for the blue dataset.

periodic structure is adopted for analysis. The stretchable part ABC consists of n parallel beams ($n = 2$ in Fig. 2(*a*)). Each beam is made up of an arc with radius R and central angle θ, and an arm with length L_1. The width of the beams is w_1. The gap width between the parallel beams is w_3 when n is more than 1. The length and width of the sensing part CD are L_2 and w_2, respectively. According to the theories in mechanics of materials [51], the relationship between the applied strain and the maximum strain of the constantan foil ε_{max} (the location is nearby point C) could be obtained analytically as (see Note S1 and Fig. S1 available in the Supplemental Materials)

$$\varepsilon_{app}$$
$$= \frac{\bar{\lambda}_1^2 \sin\theta [(\bar{\lambda}_1^2 + 4\bar{\lambda}_1 \bar{r}\theta + 6k\bar{r}^2)\sin\theta - 6k\bar{r}^2\theta\cos\theta] + n\bar{\lambda}_2(\bar{\lambda}_1 + \bar{r}\theta)}{3\bar{\lambda}_1 \sin\theta(\bar{\lambda}_1 + 2\bar{r}\theta)(\bar{\lambda}_1 \cos\theta + \bar{\lambda}_2 \bar{w} + k\bar{r}\sin\theta)} \varepsilon_{max}$$

(1)

where $\bar{r} = R/w_1$, $\bar{\lambda}_1 = L_1/w_1$, $\bar{\lambda}_2 = L_2/w_2$, $\bar{w} = w_2/w_1$, and $k = 1 - 1/(12\bar{r}^2)$ are the dimensionless geometric parameters. The elastic range of the structure $\varepsilon_{e.r.}$ is set equal to the applied strain when the maximum strain of the constantan reaches the elastic limit of constantan ($\varepsilon_{max} = 0.6\%$). Changes in dimensionless geometric

parameters may lead to changes in the stretchability of the stretchable part and, consequently, have effects on the elastic range. According to Eq. (1) with $\bar{r} = 6.25$ and $\bar{w} = 0.3125$, the effects of dimensionless parameters n, θ, $\bar{\lambda}_1$, and $\bar{\lambda}_2$ on the elastic range are studied as shown in Figs. 2(*b*)–2(*e*). It shows that a larger n induces a minor variation in the elastic range (Fig. 2(*b*)). On the other hand, the elastic range increases monotonously with increasing of θ (Fig. 2(*c*)) and $\bar{\lambda}_1$ (Fig. 2(*d*)) and decreasing of $\bar{\lambda}_2$ (Fig. 2(*e*)).

When the ISSFS is stretched, the resistance change is mainly attributed to the tensile strain of the sensing part, and the resistance change of the stretchable part and the two connection pads is negligible. With the above mechanical deformation and electrical analysis, the relative resistance change can be yielded as (see Note S2 and Fig. S2 available in the Supplemental Materials)

$$\frac{\Delta R}{R_0} = \frac{n^2(1+2\nu_{cons.})[\bar{\lambda}_2 \bar{w}\sin\theta - (n-1)(\bar{d}+1) - 1/2](\bar{\lambda}_1 + \theta\bar{r})}{\bar{w}[\bar{w}\sin\theta(\bar{\lambda}_1 + n\bar{\lambda}_2 + k\theta\bar{r}) - n(n-1)(\bar{d}+1) - n/2]} \varepsilon_{app}$$

$$\times \frac{\bar{\lambda}_1 \cos\theta + \bar{\lambda}_2 \bar{w} + k\bar{r}\sin\theta}{\bar{\lambda}_1^2 \sin\theta [(\bar{\lambda}_1^2 + 4\bar{\lambda}_1 \bar{r}\theta + 6k\bar{r}^2)\sin\theta - 6k\bar{r}^2\theta\cos\theta] + n\bar{\lambda}_2(\bar{\lambda}_1 + \bar{r}\theta)}$$

(2)

Here, R_0 and ΔR represent the initial resistance of the whole structure and the increment caused by geometric deformation, respectively. $\bar{d} = w_3/w_1$ $(n \geq 2)$ is another dimensionless geometric parameter. $\nu_{\text{cons.}}$ is Poisson's ratio of constantan. With $\bar{r} = 6.25$, $\bar{w} = 0.3125$, and $\bar{d} = 0.625$, the effects of dimensionless parameters n, θ, $\bar{\lambda}_1$, and $\bar{\lambda}_2$ on gauge factor (GF, the ratio of change in relative resistance to the applied strain) are also studied, as depicted in Figs. 2(f)–2(i). A larger n and $\bar{\lambda}_2$ results in a small rise of GF (Figs. 2(f) and 2(i)) for its minor effect on the relative stiffness, while the GF decreases monotonously with increasing of θ (Fig. 2(g)) and $\bar{\lambda}_1$ (Fig. 2(h)), which is contrary to the trends of the elastic range. The FEA results verify these analytic results with nine sets of geometric parameters (circles in Figs. 2(b)–2(i)). The design of ISSFS could be customized to meet the demands of specific applications by using the above laws of predicting the elastic range and GF.

The stretchability and linear electrical response can be understood by the deformation mechanism. When ISSFS is stretched, the overall large displacement is mainly transformed into small bending of the arc and the rotation of the arm of the wide curved segment (the stretchable part) under small deformation. In the meantime, the n-parallel-beam design $(n \geq 2)$ helps to reduce the strain level with little influence on the resistance [52]. The tensile and compressive strains caused by small bending distribute almost symmetrically on the two sides of the central axis along the direction of the potential drop, which makes the resistance change of the wide curved segment offset to about zero (Fig. 2(j)). Therefore, the wide curved segment functions as the stretchable part and has a minor resistance change. On the other hand, the narrow straight segment has a high initial resistance, and the small tensile strain results in a predominant linear resistance change. Therefore, the narrow straight segment functions as the sensing part. Although the stretchable part could be designed into other patterns, such as the serpentine [50], the current design is less prone to stress concentration and the sensing part has a clearer deformation pattern (see Note S3 available in the Supplemental Materials). Due to the combination of the two parts with different functions, there is neither unstable contact resistance nor nonlinear constitutive and geometric behavior, rendering a highly linear relationship between the applied strain and the electrical response. The high repeatability of ISSFS is ensured because all the materials just deform within the elastic limit. With $n = 3$, $\theta = 5\pi/12$, $\bar{w} = 0.3125$, and $\bar{d} = 0.625$, Fig. 2(k) compares the analytic, experimental, and FEA results of relative resistance change of three-set parameters ($\bar{\lambda}_1 = 40$ and $\bar{\lambda}_2 = 40$ for the green data set; $\bar{\lambda}_1 = 62.5$ and $\bar{\lambda}_2 = 60$ for the lavender data set; $\bar{\lambda}_1 = 62.5$ and $\bar{\lambda}_2 = 40$ for the blue data set). Results under the same parameters agree well with each other. The linearity can be quantitively defined as the coefficient of determination (R^2) of the linear fit of output signals and applied strain. Experimental results show that R^2 of the ISSFS can reach higher than 0.999, which is very close to 1, meaning that the ISSFS presents super high linearity.

2.3 Mechanical and Electrical Characterization of the Strain Sensor With Encapsulation Layers.
A complete strain sensor based on the ISSFS with encapsulation is shown in Figs. 1(a) and 1(b). A proposed sensor (detailed dimensions shown in Fig. S4 available in the Supplemental Materials) was fabricated and tested under five consecutive loading–unloading cycles under 27% applied strain. The experimental result shows that the sensor presents super high linearity ($R^2 = 0.999$) and repeatability (repeatability error [53] = 1.44%) (Fig. 3(a) and Note S4 (available in Supplemental Materials)), which is better than previous works that adopted the contact-resistance mechanism [6,8,20,54,55]. The excellent performance results from no contact resistance and linear constitutive and geometric behavior during the sensing process. Furthermore, the GF of ISSFS is relatively larger among various contact-resistance-free and stretchable structures that can be one-step patterned, such as the serpentine, the zigzag, and the

sinusoid (see Note S5 and Fig. S7 available in the Supplemental Materials). The stretchable part of the ISSFS and the three stretchable structures (the serpentine, the zigzag, and the sinusoid) are mainly in bending deformation mode when they are stretched. The tensile and compressive strains caused by bending distribute symmetrically on the two sides of the central axis, which makes the resistance change offset to zero. On the other hand, the sensing part of the ISSFS allows a tensile strain and a corresponding resistance change by the overall stretching. Attributed to the idea of independent function and the sensing part, the ISSFS could have a larger GF under the same applied strain. The GF of the sensor calibrated in Fig. 3(a) is calculated as 0.0038. The corresponding ideal error of the sensor regardless of wiring noise is about 0.089% strain (see Note S6 available in the Supplemental Materials) for the applied strain ranging from 0.5% to 30% (see Note S7 and Fig. S8 available in the Supplemental Materials) [47]. As shown in Fig. 3(b), the strain sensor can reliably distinguish a small strain of 0.5% despite fluctuations caused by noise, which is good enough for body-motion monitoring. The dynamic performance is studied in Figs. 3(c) and 3(d) and Fig. S9 (available in the Supplemental Materials). At different applied strain rates of 1.67% s^{-1}, 3.33% s^{-1}, and 8.33% s^{-1}, the sensor could derive almost the same relative resistance changes, confirming the robust output of the sensor (Fig. 3(c)). The relative resistance changes of the sensor under a loading–unloading cycle with 15%, 20%, and 25% applied strain (see Fig. S9 available in the Supplemental Materials) also verify the high linearity and repeatability of the fabricated sensor, which is consistent with the result in Fig. 3(a). When 15%, 20%, and 25% strain is applied at the strain rate of 8.33% s^{-1}, almost no overshoot occurs (Fig. 3(d)). Mechanical durability is examined by 1500 consecutive loading–unloading cycles under 20% applied strain (Fig. 3(e)). Some abnormal data at the lower and upper ends of the cycle are caused by the rapid and unstable change in the loading speed of the testing machine when the loading direction is reversed (see Note S8 and Fig. S10 available in the Supplemental Materials). The electrical response near the end of the test exhibits no noticeable drift compared to that of the beginning of the test. Such high durability and repeatability are favorable for practical applications that need multiple measurements.

Strain sensors are commonly calibrated with two ends fixed on the tensile tester, leaving the rest freestanding (mode 1, top subgraph of Fig. 3(f)). While in many practical applications, the sensors are bonded with the sensing targets and share the same strain distribution at the interface (mode 2, bottom subgraph of Fig. 3(f)). The ideal sensor should give consistent outputs under the same applied strain regardless of the stretching modes. In this case, the calibration results are applicable to the guidance of the practical tests. Experimental results suggest that the sensor (detailed dimensions shown in Fig. S11 available in the Supplemental Materials) with thin encapsulation layers would generate GFs with large disparities in two modes under the same applied strain, while the sensor with thick encapsulation layers would not (Fig. 3(g) and Fig. S12, Note S9 (available in the Supplemental Materials)). Figure 3(h) compares the FEA results of the elastic ranges in two stretching modes with different encapsulation thicknesses. As the thickness of the encapsulation layer increases, the elastic range gradually decreases in mode 1 (red lines) but increases sharply and then increases slightly in mode 2 (blue lines). In both modes, the elastic range will converge to the same stable value when the encapsulation layers are thick enough. This phenomenon can be explained by investigations of the strain distribution (Fig. S13 available in the Supplemental Materials). In mode 1, the bending of the stretchable part would be restrained by the adjacent encapsulation layers. Consequently, these are a curvature decrement at the arc and an increment at the right end of the arm, which contributes to the increase of the maximum strain of the constantan and accordingly the decrease of the elastic range. However, in mode 2, thick encapsulation layers can relieve the strong local constraint from the sensing target to the ISSFS, and the sensor with
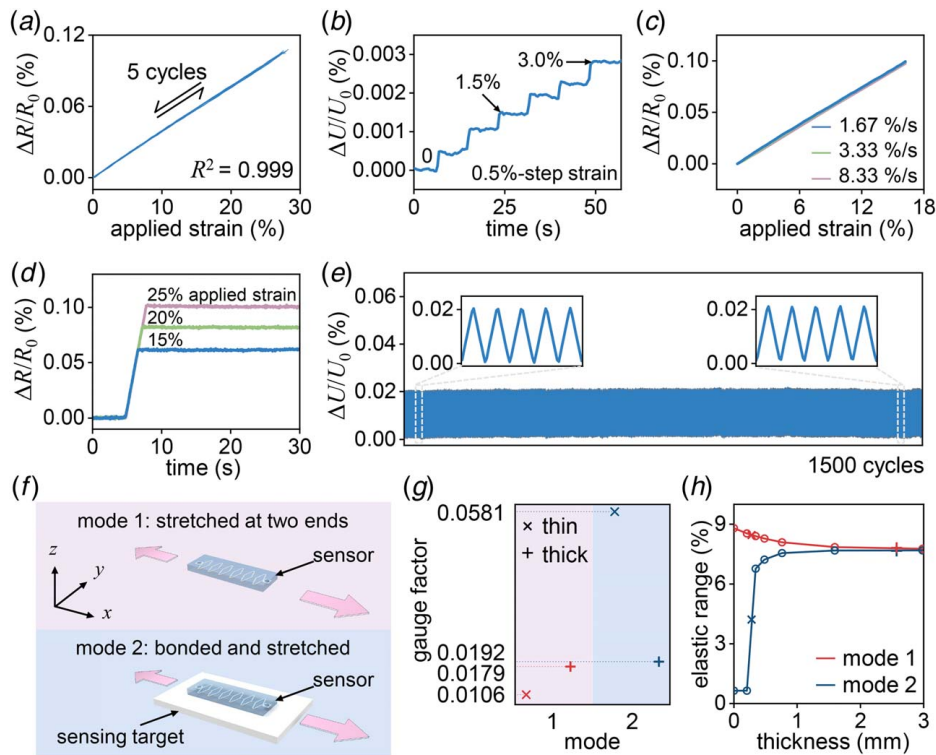
Fig. 3 Mechanical and electrical characterization of the strain sensors based on the ISSFS: (a) Relative resistance change of the sensor versus the applied strain under five consecutive loading–unloading cycles. (b) Change of the dimensionless output voltage under 0.5%-stepped applied strain (measured by a half Wheatstone bridge circuit). (c) Curves of the relative resistance change versus the applied strain with different applied strain rates. (d) Relative resistance changes for a step strain (strain rate 8.33% s^{-1}) from 0% to 15%/ 20%/25%. (e) Relative resistance change under 1500 cycles consecutive loading and unloading with 20% applied strain (measured by a half Wheatstone bridge circuit). (f) Illustration of two stretching modes. (g) Comparisons of the GF of sensors with thin and thick encapsulation layers in two modes. (h) Effects of the thickness of encapsulation layers on the elastic range in two modes.

thick encapsulation layers could have a larger elastic range than that with thin encapsulation layers. When the encapsulation layers are thick enough, the local constraint from the sensing target to the ISSFS is small and can be ignored. The strain distribution tends to be similar to that of mode 1 under the same applied strain. In this case, the sensor derives consistent outputs under the same applied strain in both modes.

2.4 Design of the Temperature Self-Compensation Structure. In practical applications, the sensing performance of strain sensors may be affected by the temperature of the environment and the sensing target. There are two common strategies to reduce the effect. One uses materials with a low temperature coefficient as sensing materials, such as the constantan (8 ppmK^{-1} at 20 °C [56]). That is, a temperature variation of 1 °C will cause a relative resistance change of 8×10^{-4}%, which is equivalent to a small effect of 0.21% applied strain for the sensor tested in Fig. 3(a). In the vast majority of wearable applications, the body surface temperature in wearable applications would not vary by more than 10 °C, which corresponds to an effect of 2% applied strain. The other relies on the design of temperature self-compensation to further reduce the influence of noise caused by temperature variation. Here, we propose a temperature self-compensation structure (TSS) integrated into the strain sensor (Fig. 4(a)), which is practical for strain measurement in a variable-temperature environment. The TSS is composed of a serpentine structure with the same material as the ISSFS, and its resistance is equal to that of the ISSFS. The deformation mechanism of the TSS is similar to that of the stretchable part of

the ISSFS, i.e., the symmetrical distribution of tensile and compressive strains along the direction of the potential drop (Fig. 4(b)) renders little resistance variation when the TSS is stretched (lavender line in Fig. 4(c)). Therefore, the GF of the TSS can be considered equal to zero. A half Wheatstone bridge circuit is built with the ISSFS and the TSS as two resistors. Figure 4(d) depicts the corresponding equivalent circuit. Here, R_1, R_2, and R_s represent the resistances of the ISSFS, the TSS and a standard resistor, respectively. U_s and U_o are the supply and output voltage, respectively. The resistances of the ISSFS and the TSS follow the linear relationship $R_i(T, \varepsilon_{app}) = R_i(T_0, 0)(1 + \alpha\Delta T)(1 + K_i\varepsilon_{app})$ when they are subjected to the applied strain ε_{app} and the temperature variation $\Delta T = T - T_0$ from the initial temperature T_0 to the current temperature T. Here, α is the temperature coefficient of resistance, the GF $K_1 \neq 0$ and $K_2 = 0$. The output voltage variation could be obtained as follows (see Note S10 available in the Supplemental Materials)

$$\Delta U = \frac{K_1 U_s}{4} \varepsilon_{app} \qquad (3)$$

The output voltage ΔU is independent of temperature items; i.e., the output of the sensor would not be affected by ambient temperature. Combining the strategies of low-temperature coefficient materials and the design of the TSS, a sensor was fabricated and tested with five consecutive loading–unloading cycles under 5% applied strain (Fig. 4(e)). The result shows the sensor with the TSS retains high linearity ($R^2 = 0.999$) and repeatability (repeatability error = 2.22%). A temperature variation experiment was also

carried out. The sensor with the TSS was placed in a temperature-controlled cabinet (Fig. S14 available in the Supplemental Materials) and underwent a 25 °C temperature increment (FLIR T420, FLIR Systems, VA, USA; Fig. 4(f)). The relative voltage output varied little (from 0 to 4.5×10^{-3}, Fig. 4(g)) after around 1200 s heating, which corresponds to less than the effect of 0.5% applied strain. The result validates the temperature self-compensation function of the TSS.

2.5 Applications in Motion Monitoring, Intelligent Devices, and Medical Treatment.

Strain variations in the human body reflect human motions and could be recorded for human–machine interactions and diagnostic aids. Figure 5(a) illustrates some potential sensing locations and corresponding motions in the human body. For instance, people who ignore their sitting posture are vulnerable to cervical spondylosis caused by prolonged head bowing. A wearable device based on the present strain sensor could be attached to the back of the neck, monitor the motion (Fig. 5(b)), and remind the user to sit straight and keep a good posture. The distinct signals of respiration at different frequencies (Fig. 5(c)) and the knee flexion and extension (Fig. 5(d)) captured by the sensor indicate its ability to record both subtle and large body motions. To keep the sensors from compression, they were pre-stretched before installation.

The strain sensor also has the potential for application in intelligent devices. For instance, a smart glove integrated with the present sensors might detect different gestures and transmit commands to the computer dynamically (Fig. 5(e)). Figure 5(f) shows the smart glove recognized bent fingers and then controlled the box in the computer (Unity 3D Software) to move right (bent finger I) and left (bent finger II). The schematic circuit of the smart glove is demonstrated in Fig. S15 (available in the Supplemental Materials). In future virtual reality (VR) systems, strain sensors may assist in sensing changes in body size due to activity, body state variation, etc. A small-size strain sensor integrated into VR devices can only be used for localized strain measurement. On the one hand, uneven skin deformation makes localized strain measurements fail to accurately catch changes in overall body size (Fig. 5(g)). On the other hand, the location

change of the small-size strain sensor caused by the slide of the device when on the skin surface could result in measurement errors (light blue line, Fig. 5(h)). Fortunately, owing to the simplicity and maturity of processing, our sensors can be fabricated longer than 30 cm (see Fig. S16 available in the Supplemental Materials) to fit snugly around the body part and successfully measure the total deformation of the upper arm (dark blue line, Fig. 5(h)). A sensing target has m different strain regions with the tensile strain, and the length of the ith region are ε_i and L_i. The total elongation can be calculated as $\Delta L = \sum_1^m L_i \varepsilon_i$. For the strain sensor whose GF $k(\varepsilon_i)$ varies with the applied strain ε_i, the electrical output $\sum_1^m L_i \cdot k(\varepsilon_i)\varepsilon_i$ cannot be used to uniquely calculate the elongation. However, with a linear electrical response, $k(\varepsilon_i)$ of our sensor is a constant K, and thus, the electrical output $K \cdot \sum_1^m L_i \varepsilon_i = K \cdot \Delta L$ of our sensor could reflect the total elongation and allow the correct evaluation of the average strain.

Tendons are soft connective tissues that withstand and transmit large forces between muscles and bones [57]. After repeated motion and degeneration, the mechanical properties of injured tendons may differ from normal ones, which could bring about long-term pain and impairment in motion function. The strain sensor could provide surgeons with quantitative information about the deformation of tendons. As a demonstration in Fig. 5(i), the sensor was attached to the Achilles tendon of a lab rabbit. The high linearity of the sensor ensures that the measurement results would not be affected by the inevitable prestrain due to installation. While the leg was driven to perform repeated movements between two different levels (ankle angle $\theta = 90$ deg and 150 deg), the sensor derived an electrical response with repetitive peaks and valleys (Fig. 5(j)). With the quantitative information about the strains of the tendon in different postures, surgeons could determine the tightness of tendons during the repair surgery and thus improve the recovery of patients' joint function.

3 Conclusion

In summary, we propose the one-step patterned contact-resistance-free stretchable strain sensors based on the
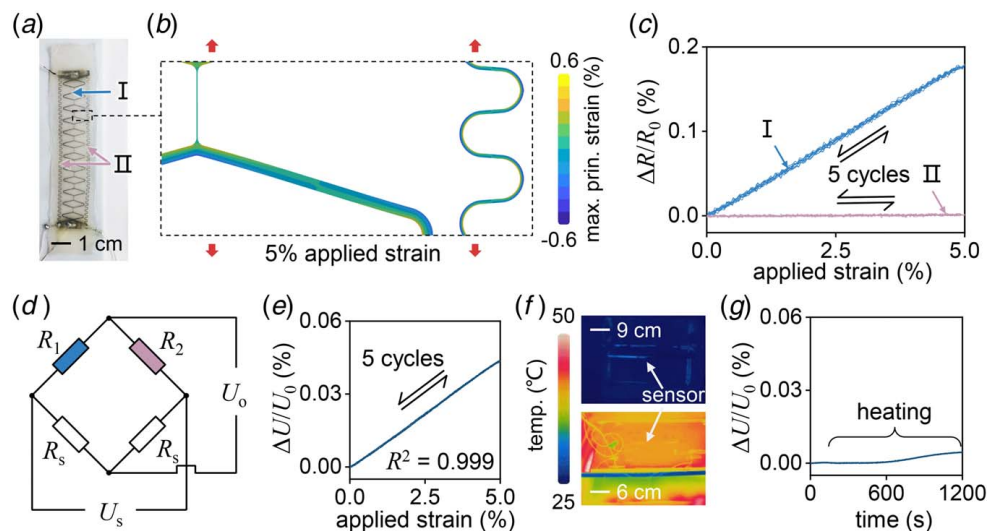

Fig. 4 (a) Optical image of a strain sensor with the TSS. (b) The maximal principal strain distribution of part of the ISSFS and the TSS. (c) Relative resistance changes of the ISSFS and the TSS versus the applied strain under five consecutive loading–unloading cycles with 5% applied strain. (d) Circuit diagram of the half Wheatstone bridge for measurement. (e) Relative voltage changes of the sensor under five consecutive loading–unloading cycles with 5% applied strain. (f) Infrared thermogram of the strain sensor placed in a temperature-controlled cabinet. Top: before heating. Bottom: after heating. (g) Relative output voltage changes during undergoing a 25 °C temperature increment.
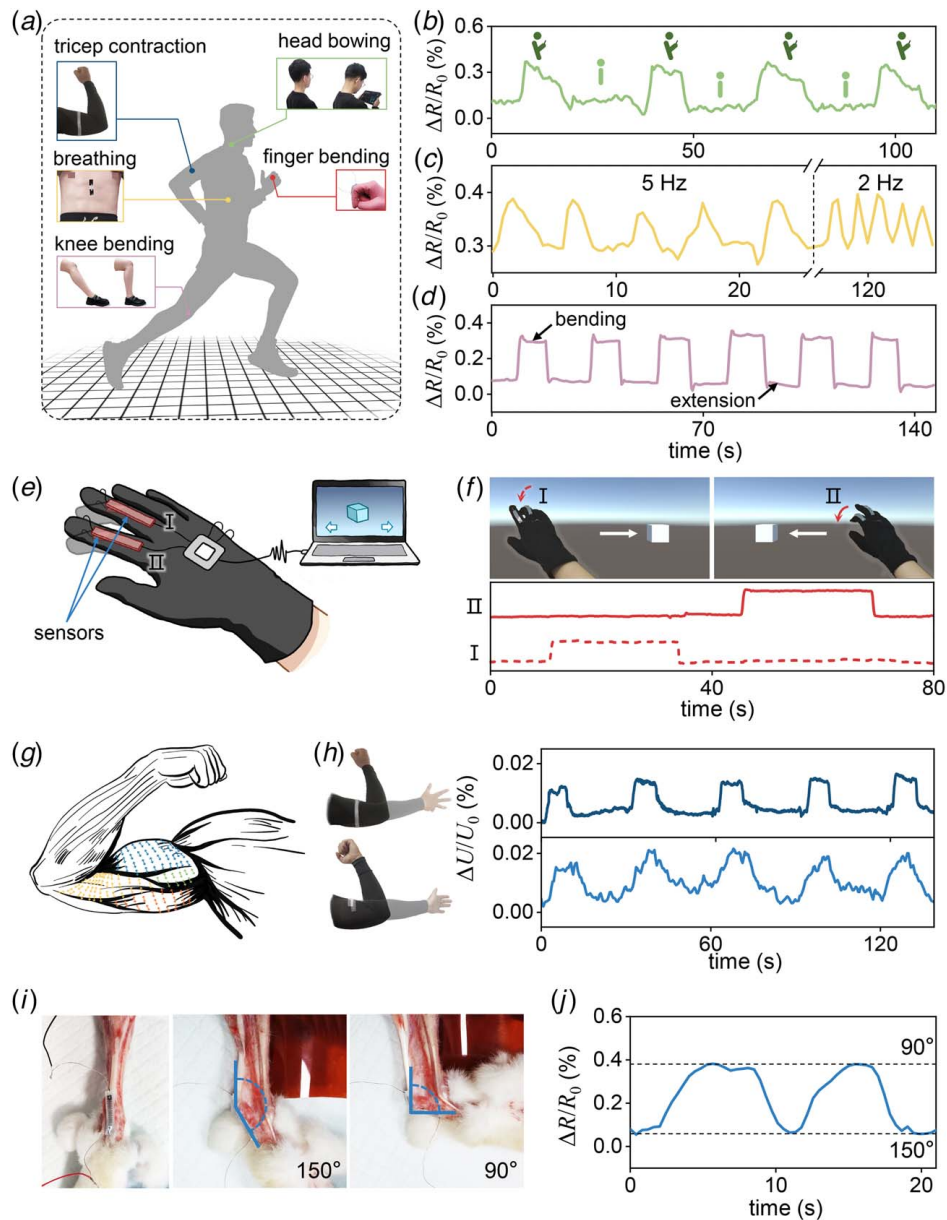
Fig. 5 (*a*) Illustration of the potential sensing locations and corresponding motions in human body. (*b*) Electrical signals of the repetitive motion of the neck. (*c*) Electrical signals of respiration at two different frequencies. (*d*) Electrical signals of the extension and bending of the knee. (*e*) Illustration of a smart glove integrated with the strain sensors and communicating with the computer. (*f*) Photographs showing the control of the box game through finger gestures and the corresponding bending signals recorded by the smart glove. (*g*) Illustration of the uneven distribution of strain on the arm. (*h*) Comparison of the electrical signals of a sensor wrapping the arm and a small-size sensor. Inset: Optical images of the sensor wrapping around the arm and the small-size sensor attached to a localized area of the arm. (*i*) Illustration of a strain sensor on the Achilles tendon of a lab rabbit and the ankle angle. (*j*) Relative resistance change of the strain sensor with repeated movements of the rabbit leg between ankle angle $\theta =$ 90 deg and 150 deg.

ISSFS. The strain sensor could have super high linearity ($R^2 =$ 0.999) and repeatability (repeatability error = 1.44%) because neither unstable contact resistance nor nonlinear constitutive and geometric behaviors would occur during the sensing process. Owing to this novel design, the conductive metal materials and the insulating substrates do not need to have different geometric layouts, and the patterning process can be completed with laser cutting in only one step. Besides, an integrated TSS is proposed and allows the sensor to eliminate the influence of the variable environment temperature. The collective results demonstrate that the

proposed strain sensor has promising applications in medical surgery, intelligent devices, and motion monitoring.

4 Experimental Section

4.1 Measurement Setup. Static/dynamic stretching tests were carried out with a programmable tensile testing machine (ZQ-990LB, ZHIQU, Dongguan, China). The strain sensors with temperature self-compensation were powered by a programmable

DC power (DP831A, RIGOL, Beijing, China). The electrical responses of the strain sensors were measured with a digital multimeter (DAQ970A, Keysight, CA, USA) for resistance variations and output voltage signals.

4.2 Finite Element Analysis of Deformation. ABAQUS/ Standard software was used for static FEA of the deformation of the ISSFS and the strain sensors with encapsulation layers. Ecoflex was regarded as the Mooney–Rivlin material [58,59] with $C_{10} = 0.00805369$ MPa, $C_{01} = 0.00201342$ MPa, and $D_1 = 2$ MPa^{-1}. PI [19,58–60] and constantan [46,61,62] were both treated as linear elastic materials with Young's modulus $E_{PI} = 2.5$ GPa and $E_{cons.} = 163$ GPa, Poisson's ratio $\nu_{PI} = 0.34$, and $\nu_{cons.} = 0.33$, respectively. C3D8RH elements modeled the encapsulation layers, and C3D8R elements were utilized for the rest. The symmetry boundaries of "XSYMM" and "YSYMM" were applied on the left and bottom cross sections, respectively. The right cross section was applied with a constant displacement load. More details can be found on Note S11 (available in the Supplemental Materials).

4.3 Finite Element Analysis of Staticelectrics. The commercial software COMSOL was adopted to solve the electrical potential distribution and resistance variation of the ISSFS with coupled multifields of solid mechanics and electric currents. The boundary conditions for the physics of solid mechanics were similar to the same as in ABAQUS. The elastic moduli were also the same as those settings in ABAQUS. For the physics of electric current, the left end of constantan was set as a 1 A current terminal, and the right end was implemented as a ground. The conductivity of constantan was set to be a constant value $\sigma_{cons.} = 2.0833 \times 10^6$ S/m. More details can be found on Note S11 (available in the Supplemental Materials).

4.4 Fabrication Process of Strain Sensors. *Step 1*: The double-layer material (Hanzhong Jingce, China) composed of a 5-μm-thick constantan foil and a 200-μm-thick PI was patterned into a structure connected in series by stretchable parts and sensing parts, by a ultraviolet picosecond laser (DL566PU, DCT, Tianjin, China). *Step 2*: The ends of the structure and copper wires were joined by solder for connection to an external circuit. *Steps 3 and 4*: Ecoflex 00-30 (Smooth-On, PA, USA) with a 1:1 mixing ratio of A to B is mixed using a magnetic stirrer at 200 rpm for 5 min. The mixture is transferred to a mold, cured at room temperature for 1 h, and forms a bottom encapsulation layer. The ISSFS is placed on the Ecoflex film and covered with a new Ecoflex mixture followed by curing.

4.5 Additional Experimental Details. The experiments involving human volunteers were approved by the Institutional Review Board at the Institute of Mechanics, Chinese Academy of Sciences (Approval No. 2022005), wherein the volunteers took part following informed consent. The animal experiments were also approved by the Institutional Review Board at Institute of Mechanics, Chinese Academy of Sciences (Approval No. 2022005).

Authorship Contribution Statement

Yuqun Lan: Conceptualization, Data curation, Formal analysis, Investigation, Methodology, Software, Visualization, Writing–original draft, Writing–review and editing. Guodong Liu: Data curation, Investigation, Methodology, Validation. Shizhen Yin: Formal analysis, Investigation, Writing–review and editing. Yang Zhao: Investigation, Software, Validation. Chong Liu: Investigation, Software. Lijuan Sun: Software. Shuang Li: Conceptualization, Data curation, Formal analysis, Methodology, Investigation, Software, Supervision, Validation, Writing–review and editing. Yewang Su:

Conflict of Interest

There are no conflicts of interest.

Data Availability Statement

The data sets generated and supporting the findings of this article are obtainable from the corresponding author upon reasonable request.

References

[1] Hong, W., Jiang, C., Qin, M., Song, Z., Ji, P., Wang, L., Tu, K., et al., 2021, "Self-Adaptive Cardiac Optogenetics Device Based on Negative Stretching-Resistive Strain Sensor," Sci. Adv., **7**(48), p. eabj4273.

[2] Mo, F., Huang, Y., Li, Q., Wang, Z., Jiang, R., Gai, W., and Zhi, C., 2021, "A Highly Stable and Durable Capacitive Strain Sensor Based on Dynamically Super-Tough Hydro/Organo-Gels," Adv. Funct. Mater., **31**(28), p. 2010830.

[3] Tan, C., Dong, Z., Li, Y., Zhao, H., Huang, X., Zhou, Z., Jiang, J.-W., et al., 2020, "A High Performance Wearable Strain Sensor With Advanced Thermal Management for Motion Monitoring," Nat. Commun., **11**(1), p. 3530.

[4] Li, L., Xiang, H., Xiong, Y., Zhao, H., Bai, Y., Wang, S., Sun, F., et al., 2018, "Ultrastretchable Fiber Sensor with High Sensitivity in Whole Workable Range for Wearable Electronics and Implantable Medicine," Adv. Sci., **5**(9), p. 1800558.

[5] Liu, Q., Chen, J., Li, Y., and Shi, G., 2016, "High-Performance Strain Sensors With Fish-Scale-Like Graphene-Sensing Layers for Full-Range Detection of Human Motions," ACS Nano, **10**(8), pp. 7901–7906.

[6] Cheng, Y., Wang, R., Sun, J., and Gao, L., 2015, "A Stretchable and Highly Sensitive Graphene-Based Fiber for Sensing Tensile Strain, Bending, and Torsion," Adv. Mater., **27**(45), pp. 7365–7371.

[7] Kang, D., Pikhitsa, P. V., Choi, Y. W., Lee, C., Shin, S. S., Piao, L., Park, B., Suh, K.-Y., Kim, T., and Choi, M., 2014, "Ultrasensitive Mechanical Crack-Based Sensor Inspired by the Spider Sensory System," Nature, **516**(7530), pp. 222–226.

[8] Amjadi, M., Pichitpajongkit, A., Lee, S., Ryu, S., and Park, I., 2014, "Highly Stretchable and Sensitive Strain Sensor Based on Silver Nanowire–Elastomer Nanocomposite," ACS Nano, **8**(5), pp. 5154–5163.

[9] Zhang, Y., Yang, J., Hou, X., Li, G., Wang, L., Bai, N., Cai, M., et al., 2022, "Highly Stable Flexible Pressure Sensors With a Quasi-Homogeneous Composition and Interlinked Interfaces," Nat. Commun., **13**(1), p. 1317.

[10] Lee, S., Franklin, S., Hassani, F. A., Yokota, T., Nayeem, O. G., Wang, Y., Leib, R., Cheng, G., Franklin, D. W., and Someya, T., 2020, "Nanomesh Pressure Sensor for Monitoring Finger Manipulation Without Sensory Interference," Science, **370**(6519), pp. 966–970.

[11] Sundaram, S., Kellnhofer, P., Li, Y., Zhu, J.-Y., Torralba, A., and Matusik, W., 2019, "Learning the Signatures of the Human Grasp Using a Scalable Tactile Glove," Nature, **569**(7758), pp. 698–702.

[12] Lee, Y., Park, J., Cho, S., Shin, Y.-E., Lee, H., Kim, J., Myoung, J., et al., 2018, "Flexible Ferroelectric Sensors With Ultrahigh Pressure Sensitivity and Linear Response Over Exceptionally Broad Pressure Range," ACS Nano, **12**(4), pp. 4045–4054.

[13] Lee, S., Reuveny, A., Reeder, J., Lee, S., Jin, H., Liu, Q., Yokota, T., et al., 2016, "A Transparent Bending-Insensitive Pressure Sensor," Nat. Nanotechnol., **11**(5), pp. 472–478.

[14] Sun, J.-Y., Keplinger, C., Whitesides, G. M., and Suo, Z., 2014, "Ionic Skin," Adv. Mater., **26**(45), pp. 7608–7614.

[15] Lu, Y., Fujita, Y., Honda, S., Yang, S.-H., Xuan, Y., Xu, K., Arie, T., Akita, S., and Takei, K., 2021, "Wireless and Flexible Skin Moisture and Temperature Sensor Sheets Toward the Study of Thermoregulator Center," Adv. Healthcare Mater., **10**(17), p. 2100103.

[16] Yamamoto, Y., Yamamoto, D., Takada, M., Naito, H., Arie, T., Akita, S., and Takei, K., 2017, "Efficient Skin Temperature Sensor and Stable Gel-Less

Sticky ECG Sensor for a Wearable Flexible Healthcare Patch," Adv. Healthcare Mater., **6**(17), p. 1700495.

[17] Ren, X., Pei, K., Peng, B., Zhang, Z., Wang, Z., Wang, X., and Chan, P. K. L., 2016, "A Low-Operating-Power and Flexible Active-Matrix Organic-Transistor Temperature-Sensor Array," Adv. Mater., **28**(24), pp. 4832–4838.

[18] Wang, P., Hu, M., Wang, H., Chen, Z., Feng, Y., Wang, J., Ling, W., and Huang, Y., 2020, "The Evolution of Flexible Electronics: From Nature, Beyond Nature, and to Nature," Adv. Sci., **7**(20), p. 2001116.

[19] Zhao, H., Kim, Y., Wang, H., Ning, X., Xu, C., Suh, J., Han, M., et al., 2021, "Compliant 3D Frameworks Instrumented With Strain Sensors for Characterization of Millimeter-Scale Engineered Muscle Tissues," Proc. Natl. Acad. Sci., **118**(19), p. e2100077118.

[20] Kim, K.-H., Hong, S. K., Ha, S.-H., Li, L., Lee, H. W., and Kim, J.-M., 2020, "Enhancement of Linearity Range of Stretchable Ultrasensitive Metal Crack Strain Sensor *via* Superaligned Carbon Nanotube-Based Strain Engineering," Mater. Horiz., **7**(10), pp. 2662–2672.

[21] Fu, X., Li, L., Chen, S., Xu, H., Li, J., Shulga, V., and Han, W., 2021, "Knitted Ti3C2T MXene Based Fiber Strain Sensor for Human–Computer Interaction," J. Colloid Interface Sci., **604**, pp. 643–649.

[22] Zhuang, M., Yin, L., Wang, Y., Bai, Y., Zhan, J., Hou, C., Yin, L., Xu, Z., Tan, X., and Huang, Y., 2021, "Highly Robust and Wearable Facial Expression Recognition via Deep-Learning-Assisted, Soft Epidermal Electronics," Research, **2021**, p. 9759601.

[23] Araromi, O. A., Graule, M. A., Dorsey, K. L., Castellanos, S., Foster, J. R., Hsu, W.-H., Passy, A. E., et al., 2020, "Ultra-Sensitive and Resilient Compliant Strain Gauges for Soft Machines," Nature, **587**(7833), pp. 219–224.

[24] Choi, S., Yoon, K., Lee, S., Lee, H. J., Lee, J., Kim, D. W., Kim, M.-S., Lee, T., and Pang, C., 2019, "Conductive Hierarchical Hairy Fibers for Highly Sensitive, Stretchable, and Water-Resistant Multimodal Gesture-Distinguishable Sensor, VR Applications," Adv. Funct. Mater., **29**(50), p. 1905808.

[25] Lee, J., Kim, S., Lee, J., Yang, D., Park, B. C., Ryu, S., and Park, I., 2014, "A Stretchable Strain Sensor Based on a Metal Nanoparticle Thin Film for Human Motion Detection," Nanoscale, **6**(20), pp. 11932–11939.

[26] Matsuhisa, N., Kaltenbrunner, M., Yokota, T., Jinno, H., Kuribara, K., Sekitani, T., and Someya, T., 2015, "Printable Elastic Conductors with a High Conductivity for Electronic Textile Applications," Nat. Commun., **6**(1), p. 7461.

[27] Boutry, C. M., Kaizawa, Y., Schroeder, B. C., Chortos, A., Legrand, A., Wang, Z., Chang, J., Fox, P., and Bao, Z., 2018, "A Stretchable and Biodegradable Strain and Pressure Sensor for Orthopaedic Application," Nat. Electron., **1**(5), pp. 314–321.

[28] Yu, Q., Ge, R., Wen, J., Du, T., Zhai, J., Liu, S., Wang, L., and Qin, Y., 2022, "Highly Sensitive Strain Sensors Based on Piezotronic Tunneling Junction," Nat. Commun., **13**(1), p. 778.

[29] Cao, X., Xiong, Y., Sun, J., Zhu, X., Sun, Q., and Wang, Z. L., 2021, "Piezoelectric Nanogenerators Derived Self-Powered Sensors for Multifunctional Applications and Artificial Intelligence," Adv. Funct. Mater., **31**(33), p. 2102983.

[30] Wang, X., Zhang, Y., Zhang, X., Huo, Z., Li, X., Que, M., Peng, Z., Wang, H., and Pan, C., 2018, "A Highly Stretchable Transparent Self-Powered Triboelectric Tactile Sensor with Metallized Nanofibers for Wearable Electronics," Adv. Mater., **30**(12), p. 1706738.

[31] Pan, L., Liu, G., Shi, W., Shang, J., Leow, W. R., Liu, Y., Jiang, Y., Li, S., Chen, X., and Li, R.-W., 2018, "Mechano-Regulated Metal–Organic Framework Nanofilm for Ultrasensitive and Anti-Jamming Strain Sensing," Nat. Commun., **9**(1), p. 3813.

[32] Huang, S., Zhang, B., Shao, Z., He, L., Zhang, Q., Jie, J., and Zhang, X., 2020, "Ultraminiaturized Stretchable Strain Sensors Based on Single Silicon Nanowires for Imperceptible Electronic Skins," Nano Lett., **20**(4), pp. 2478–2485.

[33] Ren, Y., Yang, X., Chang, Y., Shu, J., and Luo, K., 2019, "Highly Sensitive and Flexible Strain Sensor Based on Au Thin Film," J. Micromech. Microeng., **29**(1), p. 015001.

[34] Lipomi, D. J., Vosgueritchian, M., Tee, B. C.-K., Hellstrom, S. L., Lee, J. A., Fox, C. H., and Bao, Z., 2011, "Skin-Like Pressure and Strain Sensors Based on Transparent Elastic Films of Carbon Nanotubes," Nat. Nanotechnol., **6**(12), pp. 788–792.

[35] Wang, C., Li, X., Gao, E., Jian, M., Xia, K., Wang, Q., Xu, Z., Ren, T., and Zhang, Y., 2016, "Carbonized Silk Fabric for Ultrastretchable, Highly Sensitive, and Wearable Strain Sensors," Adv. Mater., **28**(31), pp. 6640–6648.

[36] Ryu, S., Lee, P., Chou, J. B., Xu, R., Zhao, R., Hart, A. J., and Kim, S.-G., 2015, "Extremely Elastic Wearable Carbon Nanotube Fiber Strain Sensor for Monitoring of Human Motion," ACS Nano, **9**(6), pp. 5929–5936.

[37] Kim, K. K., Hong, S., Cho, H. M., Lee, J., Suh, Y. D., Ham, J., and Ko, S. H., 2015, "Highly Sensitive and Stretchable Multidimensional Strain Sensor With Prestrained Anisotropic Metal Nanowire Percolation Networks," Nano Lett., **15**(8), pp. 5240–5247.

[38] Gao, Y., Guo, F., Cao, P., Liu, J., Li, D., Wu, J., Wang, N., Su, Y., and Zhao, Y., 2020, "Winding-Locked Carbon Nanotubes/Polymer Nanofibers Helical Yarn for Ultrastretchable Conductor and Strain Sensor," ACS Nano, **14**(3), pp. 3442–3450.

[39] Wan, S., Zhu, Z., Yin, K., Su, S., Bi, H., Xu, T., Zhang, H., Shi, Z., He, L., and Sun, L., 2018, "A Highly Skin-Conformal and Biodegradable Graphene-Based Strain Sensor," Small Methods, **2**(10), p. 1700374.

[40] Yamada, T., Hayamizu, Y., Yamamoto, Y., Yomogida, Y., Izadi-Najafabadi, A., Futaba, D. N., and Hata, K., 2011, "A Stretchable Carbon Nanotube Strain Sensor for Human-Motion Detection," Nat. Nanotechnol., **6**(5), pp. 296–301.

[41] Zhang, Y., Ren, E., Li, A., Cui, C., Guo, R., Tang, H., Xiao, H., et al., 2021, "A Porous Self-Healing Hydrogel With an Island-Bridge Structure for Strain and Pressure Sensors," J. Mater. Chem. B, **9**(3), pp. 719–730.

[42] Wang, Y., Yang, T., Lao, J., Zhang, R., Zhang, Y., Zhu, M., Li, X., et al., 2015, "Ultra-Sensitive Graphene Strain Sensor for Sound Signal Acquisition and Recognition," Nano Res., **8**(5), pp. 1627–1636.

[43] Choi, S., Kim, S., Kim, H., Lee, B., Kim, T., and Hong, Y., 2020, "2-D Strain Sensors Implemented on Asymmetrically Bi-Axially Pre-Strained PDMS for Selectively Switching Stretchable Light-Emitting Device Arrays," IEEE Sens. J., **20**(24), pp. 14655–14661.

[44] Zhu, G., Ren, P., Hu, J., Yang, J., Jia, Y., Chen, Z., Ren, F., and Gao, J., 2021, "Flexible and Anisotropic Strain Sensors With the Asymmetrical Cross-Conducting Network for Versatile Bio-Mechanical Signal Recognition," ACS Appl. Mater. Interfaces, **13**(37), pp. 44925–44934.

[45] Liu, N., Fang, G., Wan, J., Zhou, H., Long, H., and Zhao, X., 2011, "Electrospun PEDOT:PSS–PVA Nanofiber Based Ultrahigh-Strain Sensors With Controllable Electrical Conductivity," J. Mater. Chem., **21**(47), p. 18962.

[46] Li, S., Liu, G., Li, R., Li, Q., Zhao, Y., Huang, M., Zhang, M., et al., 2021, "Contact-Resistance-Free Stretchable Strain Sensors With High Repeatability and Linearity," ACS Nano, **16**(1), pp. 541–553.

[47] Li, S., Liu, G., Wang, L., Fang, G., and Su, Y., 2020, "Overlarge Gauge Factor Yields a Large Measuring Error for Resistive-Type Stretchable Strain Sensors," Adv. Electron. Mater., **6**(11), p. 2000618.

[48] Gao, Y., Yan, C., Huang, H., Yang, T., Tian, G., Xiong, D., Chen, N., et al., 2020, "Microchannel-Confined MXene Based Flexible Piezoresistive Multifunctional Micro-Force Sensor," Adv. Funct. Mater., **30**(11), p. 1909603.

[49] Wang, S., Deng, W., Yang, T., Tian, G., Xiong, D., Xiao, X., Zhang, H., et al., 2023, "Body-Area Sensor Network Featuring Micropyramids for Sports Healthcare," Nano Res., **16**(1), pp. 1330–1337.

[50] Su, Y., Ping, X., Yu, K. J., Lee, J. W., Fan, J. A., Wang, B., Li, M., et al., 2017, "In-Plane Deformation Mechanics for Highly Stretchable Electronics," Adv. Mater., **29**(8), p. 1604989.

[51] Timoshenko, S., 1986, *Strength of Materials*, CBS Publishers & Distributors, Delhi.

[52] Brosteaux, D., Axisa, F., Gonzalez, M., and Vanfleteren, J., 2007, "Design and Fabrication of Elastic Interconnections for Stretchable Electronic Circuits," IEEE Electron Device Lett., **28**(7), pp. 552–554.

[53] Figliola, R. S., and Beasley, D. E., 2012, *Theory and Design for Mechanical Measurements*, Wiley, New York.

[54] Lee, J., Lim, M., Yoon, J., Kim, M. S., Choi, B., Kim, D. M., Kim, D. H., Park, I., and Choi, S.-J., 2017, "Transparent, Flexible Strain Sensor Based on a Solution-Processed Carbon Nanotube Network," ACS Appl. Mater. Interfaces, **9**(31), pp. 26279–26285.

[55] Song, Z., Li, W., Bao, Y., Han, F., Gao, L., Xu, J., Ma, Y., Han, D., and Niu, L., 2018, "Breathable and Skin-Mountable Strain Sensor with Tunable Stretchability, Sensitivity, and Linearity via Surface Strain Delocalization for Versatile Skin Activities' Recognition," ACS Appl. Mater. Interfaces, **10**(49), pp. 42826–42836.

[56] O'Malley, J., 1992, *Schaum's Outline of Theory and Problems of Basic Circuit Analysis*, McGraw-Hill, New York.

[57] Lin, T. W., Cardenas, L., and Soslowsky, L. J., 2004, "Biomechanics of Tendon Injury and Repair," J. Biomech., **37**(6), pp. 865–877.

[58] Won, S. M., Wang, H., Kim, B. H., Lee, K., Jang, H., Kwon, K., Han, M., et al., 2019, "Multimodal Sensing With a Three-Dimensional Piezoresistive Structure," ACS Nano, **13**(10), pp. 10972–10979.

[59] Park, Y., Kwon, K., Kwak, S. S., Yang, D. S., Kwak, J. W., Luan, H., Chung, T. S., et al., 2020, "Wireless, Skin-Interfaced Sensors for Compression Therapy," Sci. Adv., **6**(49), p. eabe1655.

[60] Jeong, H., Lee, J. Y., Lee, K., Kang, Y. J., Kim, J.-T., Avila, R., Tzavelis, A., et al., 2021, "Differential Cardiopulmonary Monitoring System for Artifact-Canceled Physiological Tracking of Athletes, Workers, and COVID-19 Patients," Sci. Adv., **7**(20), p. eabg3092.

[61] Cai, L., Burton, A., Gonzales, D. A., Kasper, K. A., Azami, A., Peralta, R., Johnson, M., et al., 2021, "Osseosurface Electronics—Thin, Wireless, Battery-Free and Multimodal Musculoskeletal Biointerfaces," Nat. Commun., **12**(1), p. 6707.

[62] Zhao, Y., Wang, Z., Tan, S., Liu, Y., Chen, S., Li, Y., and Hao, Q., 2022, "Dependance of Gauge Factor on Micro-Morphology of Sensitive Grids in Resistive Strain Gauges," Micromachines, **13**(2), p. 280.

[63] Li, J., Li, S., and Su, Y., 2022, "Stretchable Strain Sensors Based on Deterministic-Contact-Resistance Braided Structures With High Performance and Capability of Continuous Production," Adv. Funct. Mater., **32**(49), p. 2208216.

[64] Wu, S., Moody, K., Kollipara, A., and Zhu, Y., 2023, "Highly Sensitive, Stretchable, and Robust Strain Sensor Based on Crack Propagation and Opening," ACS Appl. Mater. Interfaces, **15**(1), pp. 1798–1807.

[65] Bao, M., 2005, "Introduction to MEMS Devices," *Analysis and Design Principles of MEMS Devices*, Elsevier, pp. 1–32.

[66] Bajpai, P., 2018, "Process Control," *Biermann's Handbook of Pulp and Paper*, Elsevier, pp. 483–492.

[67] Lee, K.-H., Fu, D. K. C., Leong, M. C. W., Chow, M., Fu, H.-C., Althoefer, K., Sze, K. Y., Yeung, C.-K., and Kwok, K.-W., 2017, "Nonparametric Online Learning Control for Soft Continuum Robot: An Enabling Technique for Effective Endoscopic Navigation," Soft Robot., **4**(4), pp. 324–337.

[68] Hughes, T. J. R., 2000, *The Finite Element Method: Linear Static and Dynamic Finite Element Analysis*, Dover Publications, Mineola, NY.